Preparation of hematite with an ultrathin iron titanate layer via an in situ reaction and its stable, long-lived, and excellent photoelectrochemical performance

Shuai Chen [a,1], Qingyi Zeng [a,1], Jing Bai [a], Jinhua Li [a,*], Linsen Li [a], Ligang Xia [a], Baoxue Zhou [a,b,*]

[a] School of Environmental Science and Engineering, Shanghai Jiao Tong University, No. 800 Dongchuan Rd., Shanghai, PR China
[b] Key Laboratory of Thin Film and Microfabrication Technology, Ministry of Education, Shanghai 200240, PR China

ARTICLE INFO

ABSTRACT

In this work, a facile and in situ method is proposed to prepare a high-performance photoanode with an ultrathin Fe$_2$TiO$_5$ layer on hematite by the reaction of tetrabutyl titanate with electro-reduced Fe film, which avoids using FeOOH film as substrate. The preparation involves 30 s of direct electro-reduction (ER) of Fe film and 3 min of a sol method, followed by thermal treatment. The as-prepared photoanode shows a significant enhancement of the photocurrent density to ~2.0 mA/cm^2 (1.23 V vs. RHE). The incorporation of a Co/Pi catalyst resulted in a photocurrent density of ~3.05 mA/cm^2. The high photoelectrochemical performance can be attributed to the low microstructural defects, the better carrier separation and faster electron transfer based on electrochemical impedance spectroscopy (EIS) and Intensity-modulated photocurrent spectroscopy (IMPS) analysis. In addition, the prepared photoanode shows good stability under both alkaline and neutral conditions.

© 2017 Elsevier B.V. All rights reserved.

1. Introduction

To address the environmental degradation occurring worldwide and the energy shortage crisis, photoelectrocatalytic (PEC) methods have emerged as promising techniques because of their cleanness, non-polluting nature and high efficiency. Since Fujishima and Honda published their work on the electrochemical photolysis of water in 1972, substantial attention has been directed toward the process by which PEC systems split water and degrade organic pollutants [1–4]. Researchers have determined that photoelectrodes play a key role during this process, connecting solar energy and environmental receptors [5]. Many types of photoelectrodes, especially semiconductor metal oxides, such as TiO$_2$, Fe$_2$O$_3$ and WO$_3$ have been developed and evaluated [6–8].

As one of the most favorable optical band gap (2.0 eV) materials, hematite (α-Fe$_2$O$_3$) has attracted abundant research interest [8,9]. Indeed, this material is not only non-polluting and environmentally benign but also inexpensive and alkaline stable [8–11]. Because

of its low band gap, it can use 40% of the energy of the visible light spectrum to excite electrons, and theoretically, its solar-to-hydrogen efficiency can reach 16.8% [8,12]. However, in reality, hematite presents a series of drawbacks that limit its PEC activity during practical application, including a high carrier recombination rate, short carrier lifetime, short holes diffusion length and poor conductivity [8]. In addition, a relatively high external bias is needed to achieve water reduction because the conduction band of hematite is lower than the water reduction potential [12]. All these defects are the obstacles to limit its electrochemical engineering applications. To address some of these issues, the primary modification strategies used are nanostructuring [12–14], ion doping [15–17] and surface modification [18,19]. Among these, establishing heterojunctions with co-catalysts or other photocatalysts is of key interest because this strategy could effectively transfer and separate charge in the bulk related to the internal potential caused by band interleaving [20]. Herein, we seek a stable and low-cost photocatalyst with an appropriate band structure for combination with hematite and also consider its crystalline structure and interfacial properties with hematite.

Currently, Fe$_2$TiO$_5$ is attracting increased attention largely because of its excellent thermodynamic stability; its natural energy band, which exactly spans the water redox potential [21,22]; its

---

* Corresponding authors at: School of Environmental Science and Engineering, Shanghai Jiao Tong University, No. 800 Dongchuan Rd., Shanghai, PR China.
E-mail addresses: lijinhua@sjtu.edu.cn (J. Li), zhoubaoxue@sjtu.edu.cn (B. Zhou).
[1] Shuai Chen and Qingyi Zeng are equally contributed to this work.

narrow bandgap (∼2.1 eV); and its low cost. All these advantages make the combination of Fe_2O_3 and Fe_2TiO_5 feasible. Moreover, data have shown that the Fe_2O_3/Fe_2TiO_5 heterojunction shows the expected high photoelectrical performance with effective charge separation and transfer compared to pristine hematite [23]. Up to now, a few number of Fe_2O_3/Fe_2TiO_5 structure have been reported for photo-driven water splitting based on FeOOH film coated with titanium compounds on the surface, followed by thermal treatment. For instance, Deng et al. used $TiCl_4$ vapor deposition or a simple HF-assisted Ti-based treatment on FeOOH substrate to synthesize a thin Fe_2TiO_5 layer on hematite [19]. Li et al. prepared a similar Fe_2O_3/Fe_2TiO_5 structure by depositing a TiO_2 ultrathin film over hydrothermal FeOOH nanorods (NRs) substrate through atomic layer deposition (ALD) [22]. Bassi et al. constructed ɑ-Fe_2O_3/Fe_2TiO_5 photoanode by initially fabricating ɑ-Fe_2O_3 nanorods through FeOOH and subsequently Fe_2TiO_5 nanoporous thin film on top of them [23]. Although these works clearly highlighted the feasibility to prepare ɑ-Fe_2O_3/Fe_2TiO_5 photoelectrode with a considerable enhancement in photocurrent density, the routes for preparing photoelectrode should be unsatisfactory because the FeOOH substrate has to be used. In fact, it is easy to cause undesirable microstructural defects in the FeOOH substrate, since a variety of species of Fe^{3+} are formed in aqueous solution, including polyhydroxy complexes and bridging ligands in the formation process of FeOOH film, and these microstructural defects should be also then present in the final ɑ-Fe_2O_3/Fe_2TiO_5 structure. In addition, although ALD allows for a controllable Fe_2TiO_5 coating layer, this technique remains quite expensive.

Here, for the first time we report a simple and in situ method to prepare a high-performance ɑ-Fe_2O_3 photoanode with an ultrathin Fe_2TiO_5 layer by the reaction of tetrabutyl titanate (TT) with electro-reduced Fe film to avoid using FeOOH film as substrate. First, a uniform iron film is deposited on the conductive substrate by direct electro-reduction (ER). Compared to FeOOH, both microstructural defects and unwanted impurities are absent. Second, an ultrathin TT is coated on iron film directly by sol method that the Fe/TT structure was constructed. Finally, the Fe/TT structure completely converted to ɑ-Fe_2O_3/Fe_2TiO_5 after thermal treatment in air. Integrating these three low-cost and convenient preparation processes formed a uniform hematite with an ultrathin Fe_2TiO_5 layer that showed excellent photoelectrochemical performance with a considerable enhancement in photocurrent density ca.2.0 mA/cm^2, which is significantly better than previous results reported in literature [19,22,23]. The incorporation of a Co/Pi catalyst resulted in a photocurrent density of ∼3.05 mA/cm^2. The high photoelectrochemical performance can be attributed to the lower microstructural defects, the faster electron transfer and the better carrier separation by avoiding the use of FeOOH substrate, based on electrochemical impedance spectroscopy (EIS) and Intensity-modulated photocurrent spectroscopy (IMPS) analysis. In addition, the prepared ɑ-Fe_2O_3/Fe_2TiO_5 shows good continuous stability under neutral and alkaline conditions in 60 h continuous operation, while the ɑ-Fe_2O_3 shows intermittent significant attenuation by 47.5% in photocurrent intensity under neutral condition.

In summary, the novel facile method proposed here can greatly enhance the performance and lifetime of hematite and reduce preparation costs, making large-scale preparation possible.

2. Experimental

2.1. Synthesis of ɑ-Fe_2O_3 film

The Fe film was first electro-reduced on an F-doped tin oxide (FTO)-coated glass substrate (13 Ω cm^{-1}) in a two-electrode configuration, with the FTO glass acting as the cathode and a platinum foil

as the anode. The distance between the cathode and the anode was 3 cm. The electrolyte was prepared by dissolving 5 g of $FeSO_4·7H_2O$ and 30 mL of ammonia (27%) in 150 mL of deionized water, giving a pH of 10.8 at 25 °C. The ER process was conducted at 2 V for 30 s with vigorous stirring. The deposited Fe film was rinsed with deionized water for 5 min and dried at 50 °C in a gentle stream of nitrogen for 1 h, followed by thermal oxidation in air at 500 °C for 2 h and 700 °C for 10 min.

2.2. Synthesis of ɑ-Fe_2O_3/Fe_2TiO_5 film

The sol method was used to prepare the Ti-based coating layer on the as-prepared deposited Fe film. TT sol was prepared by adding TT to 60 mL of absolute ethanol with vigorous stirring. To eliminate performance differences between samples of the as-prepared Fe film, we cut the Fe film sample (30 mm × 30 mm) in half (15 mm × 30 mm) using a glasscutter. One half was immersed in the TT sol for 3 min and dried at 50 °C in a gentle stream of nitrogen for 1 h, and both samples were annealed in air at 500 °C for 2 h and 700 °C for 10 min. As a control, ɑ-Fe_2O_3/TiO_2 samples were prepared by subjecting the Fe film to an additional thermal treatment step in air at 500 °C for 2 h and 700 °C for 10 min, followed by the above sol-gel method. The synthesis of ɑ-Fe_2O_3/TiO_2 was performed to prevent interface reactions and, thus, stably form ɑ-Fe_2O_3 and TiO_2. The cutting method was utilized in all cases.

The deposition of Co-Pi on the surface of the ɑ-Fe_2O_3/Fe_2TiO_5 was achieved via a photo-assisted electrodeposition method using a three-electrode system and 0.1-M potassium phosphate buffer solution containing 0.5-mM cobaltous nitrate (pH 7) as a electrolyte. The deposition process was conducted at 0.15 V vs. Ag/AgCl for 500 s under AM 1.5 illumination, followed by rinsing with deionized water for 5 min and drying at 50 °C in a gentle stream of nitrogen for 1 h.

2.3. Synthesis of Fe_2TiO_5 film

As reported by Kozuka et al. [25], a solution of molar compositions, $Fe(NO_3)_3·9H_2O$: $Ti(OC_3Hi_7)_4$: $CH_3COCH_2COCH_3$: $CH_3OC_2H_4OH$: $H_2O = 2:1:4:20:26$ was prepared by adding $Ti(OC_3Hi_7)_4$ to $CH_3COCH_2COCH_3$—$CH_3OC_2H_4OH$ solution and then adding $Fe(NO_3)_3·9H_2O$. A deep brown solution was obtained. A FTO (30 × 30 mm) was immersed into the solution for 10 min, then annealed at 700∘C for 10 min.

2.4. Structural characterization

The surface morphology and structure were determined by field emission scanning electron microscopy (FE-SEM; Nova NanoSEM 450, FEI Company, USA). The microstructure and elemental composition were further investigated by high-resolution transmission electronic microscopy (HRTEM; JEM2100F, JEOL Ltd., Japan) equipped with an energy-dispersive X-ray detector (EDX). X-ray diffractometry (XRD; AXS-8 Advance, Bruker, Germany) and X-ray photoelectron spectrometry (XPS; AXIS UltraDLD, Kratos, Japan) were applied for structural characterization. Raman spectra were collected on a Senterra R200 (Bruker, Germany). Ultraviolet (UV)–vis absorption spectra were recorded on a UV–vis spectrophotometer (TU1900, Beijing Purkinje General Instrument Co, China) with an integrating sphere.

2.5. Photoelectrochemical measurements

The PEC water splitting measurements were conducted using a three-electrode system and an electrochemical workstation (CHI 660D, CH Instruments Inc., USA) in 1-M KOH electrolyte. Prior to measurement, the electrolyte was purged with N_2 for 30 min. A

platinum foil was used as the auxiliary electrode, and an Ag/AgCl electrode was used as the reference electrode. The light source was a 350-W xenon lamp (Shanghai Hualun Bulb Factory) equipped with an AM 1.5 filter (light density, 100 mW/cm^2). The potential scan rate was 50 mV s^{-1}. The measured potentials of the Ag/AgCl electrode were converted to the RHE scale according to the following formula: $E_{RHE} = E_{Ag/AgCl} + 0.0591 \times pH + 0.1976$.

The incident photon-to-charge conversion efficiency (IPCE) was measured using a monochromator (Zolix, China) equipped with a 500-W xenon arc lamp, a calibrated silicon photodetector and a power meter. IPCE data were collected from 300 to 700 nm at 1.23 V vs. RHE and can be described by:

$$IPCE\,(100\%) = \frac{1240\,(Vnm) \times \left[j\,\left(mAcm^{-2} \right) \right]}{P\,\left(mWcm^{-2} \right) \times \lambda\,(nm)}$$

where P is the monochromated illumination power density at a specific wavelength.

Electrochemical impedance spectroscopy (EIS) was performed using the same electrochemical workstation and three-electrode system used for the photocurrent measurements with the following testing conditions: amplitude perturbations of 5 mV, a frequency range of 1 Hz to 10 kHz, and specific direct current constant potentials (0.7–1.3 V vs. RHE). Using the Zsimpwin software (v. 3.10), Nyquist plots were fitted to the selected equivalent circuits (ECs). Mott-Schottky plots were obtained from 0 to 2 V vs. RHE at 1 kHz in the dark.

Intensity-modulated photocurrent spectroscopy (IMPS) was performed using an electrochemical workstation (Zennium; effect-Elektrik, Germany) coupled to a controlled intensity-modulated photospectroscopy set-up (CIMPS, PP211) and a white-light lamp (WLC02; Zahner-Elektrik) whose DC illumination was adjusted to 80 mW/cm^2, with 1-M KOH electrolyte at 1.23 V vs. RHE. The same three-electrode configuration was used, with the prepared film as the working electrode, a platinum foil as the counter electrode, and a saturated calomel electrode (SCE) as the reference electrode. Modulated light in the frequency range of 0.1–10 kHz was applied.

3. Results and discussion

3.1. Structural characterization

Two basic and facile methods of synthesizing materials were used in this work (Fig. 1): cathodic ER for the preparation of Fe films on FTO substrates and the sol method for Ti-based deposition on Fe films, followed by annealing in air. A uniform and orderly Fe film is deposited during the ER process because of both the absence of undesired FeO and/or Fe$_3$O$_4$ phases and the stability of the Fe film [24]. An ultrathin TT layer is then formed on the Fe film by immersing the sample into TT solution for 3 min. Subsequently, the as-prepared sample is initially annealed at 500 °C to stably convert the Fe film into hematite and simultaneously obtain the iron-titanium oxides. Then, it is further annealed at 700 °C to increase the width of the space charge layer and, thereby, reduce the combination of photoexcited electrons and holes [25]. SEM was used to investigate the surface morphology and crystal structure of α-Fe$_2$O$_3$ and α-Fe$_2$O$_3$/Fe$_2$TiO$_5$. The top-view SEM images of pristine hematite and α-Fe$_2$O$_3$/Fe$_2$TiO$_5$ samples are shown in Fig. 2. All the samples show a compact state with a relatively smooth surface consisting of nanoparticles, with no significant differences in surface morphology between the pristine hematite and α-Fe$_2$O$_3$/Fe$_2$TiO$_5$, possibly because of the ultrathin Fe$_2$TiO$_5$ coating layer. These results only confirm the existence of a hematite film with a thickness of approximately 195 nm, as shown in the cross-sectional image (Fig. S1). Based on the HRTEM images of corresponding samples shown in Fig. 2(C) and (D), an apparent surface coating layer with a thickness of approximately 7 nm can be observed on α-Fe$_2$O$_3$/Fe$_2$TiO$_5$ compared to pristine hematite.

The XRD spectra of α-Fe$_2$O$_3$, α-Fe$_2$O$_3$/TiO$_2$ and α-Fe$_2$O$_3$/Fe$_2$TiO$_5$ are shown in Fig. 3(A). The characteristic peaks of hematite (JCPDS no. 890598) and the SnO$_2$ substrate are clearly evident, confirming the existence of hematite and FTO. Upon TT deposition, the hematite peak remains substantially unchanged, indicating that the Ti-based compound has no effect on the formation of hematite. However, because of the thinner Fe$_2$TiO$_5$ layer, no additional peak arises, and thus, further investigation of its physicochemical characteristics is required.

XPS was performed to detect the constituent elements and corresponding valence and chemical bonding [26]. The XPS scan spectra of α-Fe$_2$O$_3$/Fe$_2$TiO$_5$ shown in Fig. 3(B) display peaks of Fe 2p, O 1s, Ti 2p and C 1s, indicating the presence of Fe, O, Ti and C in the sample; however, the Ti peak is too small to distinguish. The existence of C could be ascribed to organic or inorganic carbon pollution in the samples, including carbon impurities introduced during the experiment and the deposition of atmospheric carbon dioxide. The high-resolution spectra in Fig. S2 shows the Fe 2p orbital spectra of pristine hematite and post-deposition film, with two distinct peaks of Fe 2p$_{3/2}$ and Fe 2p$_{1/2}$; no peak shift or change in intensity can be identified. Characteristic satellite peaks of α-Fe$_2$O$_3$ are also detected at 719.26 and 718.98, revealing that Fe is present as Fe^{3+} in both samples [27]. Notably, the energy separations between Fe 2p$_{3/2}$ and the satellite peaks are 8.5 eV and 8.4 eV (Fig. S3), which are in good agreement with the reported energy of α-Fe$_2$O$_3$ with a highly electronegative oxygen ligand [27]. In Fig. 3(B) (high-resolution spectra), the peaks of both Ti 2p$_{3/2}$ and Ti 2p$_{1/2}$ of α-Fe$_2$O$_3$/Fe$_2$TiO$_5$ center at 463.67 eV and 458.27 eV, respectively, clearly confirming the existence of Ti. Additionally, the spin orbit splitting energy between Ti 2p$_{3/2}$ and Ti 2p$_{1/2}$ is 5.4 eV, implying that the Ti^{4+} oxidation state is present in the film [28].

Based on the above test results, Raman spectra were collected to further investigate the formation of iron and titanium oxides. Fig. 3(C) shows the Raman spectra of α-Fe$_2$O$_3$ and α-Fe$_2$O$_3$/Fe$_2$TiO$_5$. The characteristic peaks of α-Fe$_2$O$_3$ are located at 224, 242.5, 291.5, 408, 499, and 608 cm^{-1}, in accordance with previous work [29]. Notably, the peak at 656 cm^{-1} (black line), which is also known as the characteristic peak of α-Fe$_2$O$_3$ [30], shows a relatively significant enhancement in its intensity and a slight redshift (from 656 to 660 cm^{-1}) after TT deposition. This peak was previously considered the only one sensitive to the substitution of Fe by other elements and could be used as a probe for some elements (e.g., titanium) that affect the hematite lattice [30]. Thus, the peak at 660 cm^{-1} could signify the existence of Fe$_2$TiO$_5$ resulting from a similar process as that occurring in titanium-iron oxide [32,33]. Therefore, the peaks at 660 cm^{-1} of the two Ti-deposited films can be treated as a combination of the characteristic peaks of both compounds. Moreover, the characteristic peak of Fe$_2$TiO$_5$ appears at 792 cm^{-1}, and no TiO$_2$ peak is observed [34]. For comparison, Fig. S4 presents the Raman spectra of α-Fe$_2$O$_3$/TiO$_2$, clearly showing the TiO$_2$ peak of at 146 cm^{-1} and the Fe$_2$TiO$_5$ peak [34].

As a narrow band gap semiconductor, α-Fe$_2$O$_3$ has excellent light absorption properties and can absorb light at wavelengths below 590 nm. This was confirmed by the UV–vis absorption spectra presented in Fig. 3(D) (black line). Compared to α-Fe$_2$O$_3$, α-Fe$_2$O$_3$/Fe$_2$TiO$_5$ shows relatively weak absorption intensity, although the Fe$_2$TiO$_5$ is very thin. All the samples exhibit the same absorption region below 590 nm, indicating a similar bandgap of approximately 2.0–2.1 eV (Fig. S4. Including pure Fe$_2$TiO$_5$ and α-Fe$_2$O$_3$/TiO$_2$). As a control, α-Fe$_2$O$_3$/TiO$_2$ shows lower absorption intensity because of the large band gap of the TiO$_2$ coated on the α-Fe$_2$O$_3$ film (Fig. S4).
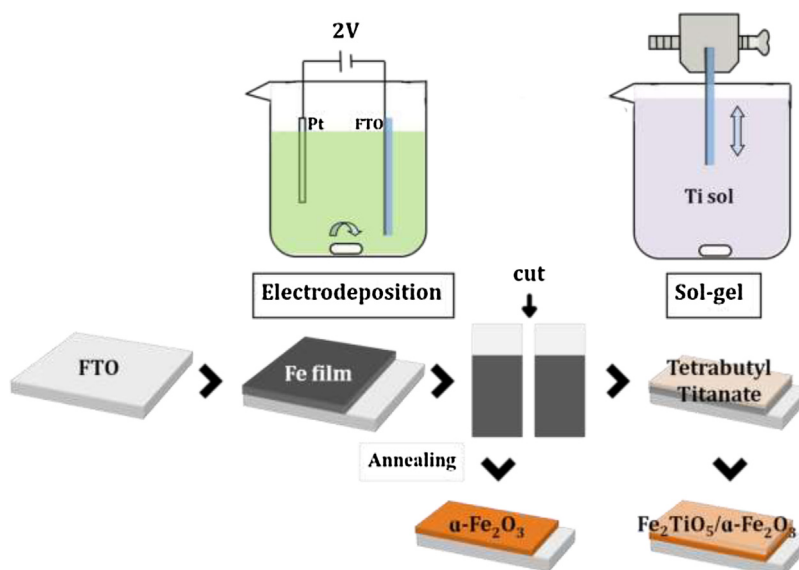
Fig. 1. A schematic illustration of the synthesis process of Ti-deposited hematite and pristine hematite under the same annealing conditions.
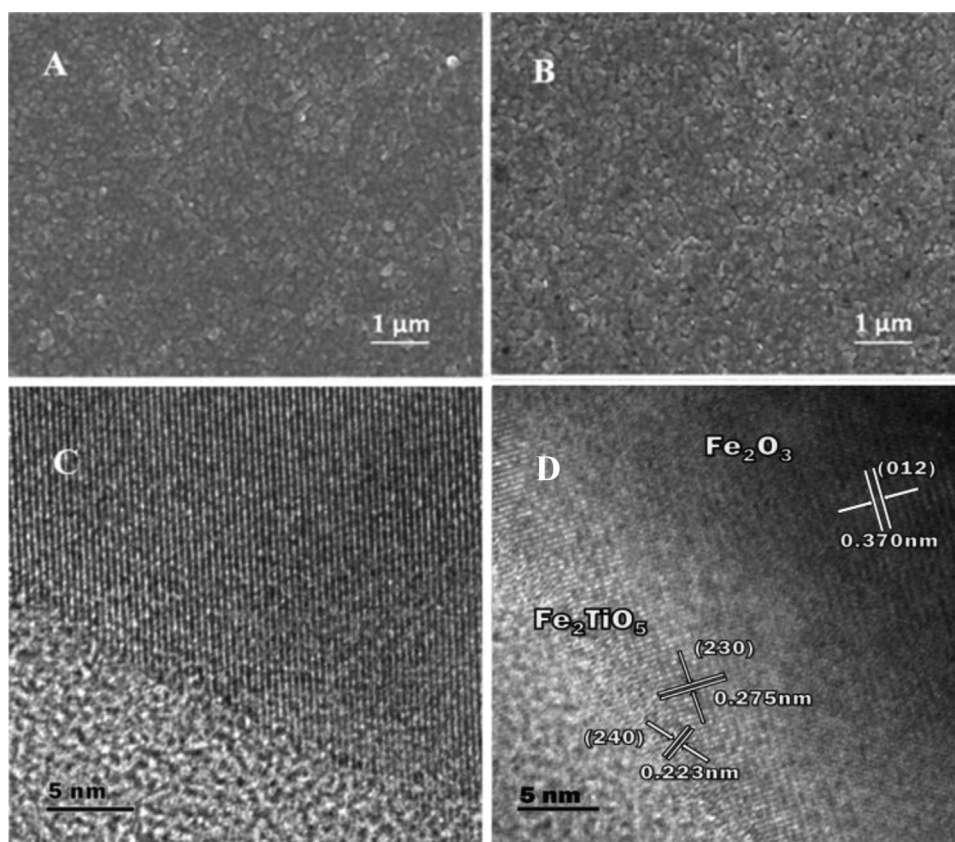

Fig. 2. Top-view SEM images of pristine hematite (A) and α-Fe$_2$O$_3$/Fe$_2$TiO$_5$ (B). HRTEM images of corresponding α-Fe$_2$O$_3$/Fe$_2$TiO$_5$ samples (C, D) in A and B. Both α-Fe$_2$O$_3$ and α-Fe$_2$O$_3$/Fe$_2$TiO$_5$ were sintered at 500 °C for 2 h and 700 °C for 10 min.

3.2. Photoelectrochemical characterizations

To illustrate the effect of the deposited Fe$_2$TiO$_5$ layer on the photoelectrical properties, chopped photocurrent-potential curves of α-Fe$_2$O$_3$, α-Fe$_2$O$_3$/TiO$_2$, α-Fe$_2$O$_3$/Fe$_2$TiO$_5$ and α-Fe$_2$O$_3$/Fe$_2$TiO$_5$/Co-Pi are shown in Fig. 4(A). The deposited Fe$_2$TiO$_5$ layer clearly exhibits a significant positive effect on the performance of α-Fe$_2$O$_3$, which increases from 0.7 mA cm^{-2} to 2.0 mA cm^{-2} at 1.23 V vs. RHE.

Unlike the loose nanostructures of hematite, compact hematite has the advantages of the absence of microstructural defects that impede the transportation of carriers and the presence of the deposited Fe$_2$TiO$_5$ layer that further enhances electrode-hole pair transfer and separation, causing a larger photocurrent density of 2.0 mA cm^{-2} than previously reported α-Fe$_2$O$_3$/Fe$_2$TiO$_5$ [23]. As we predicted, the very low photocurrent value of α-Fe$_2$O$_3$/TiO$_2$ compared to that of α-Fe$_2$O$_3$ implies that TiO$_2$ impedes holes trans-
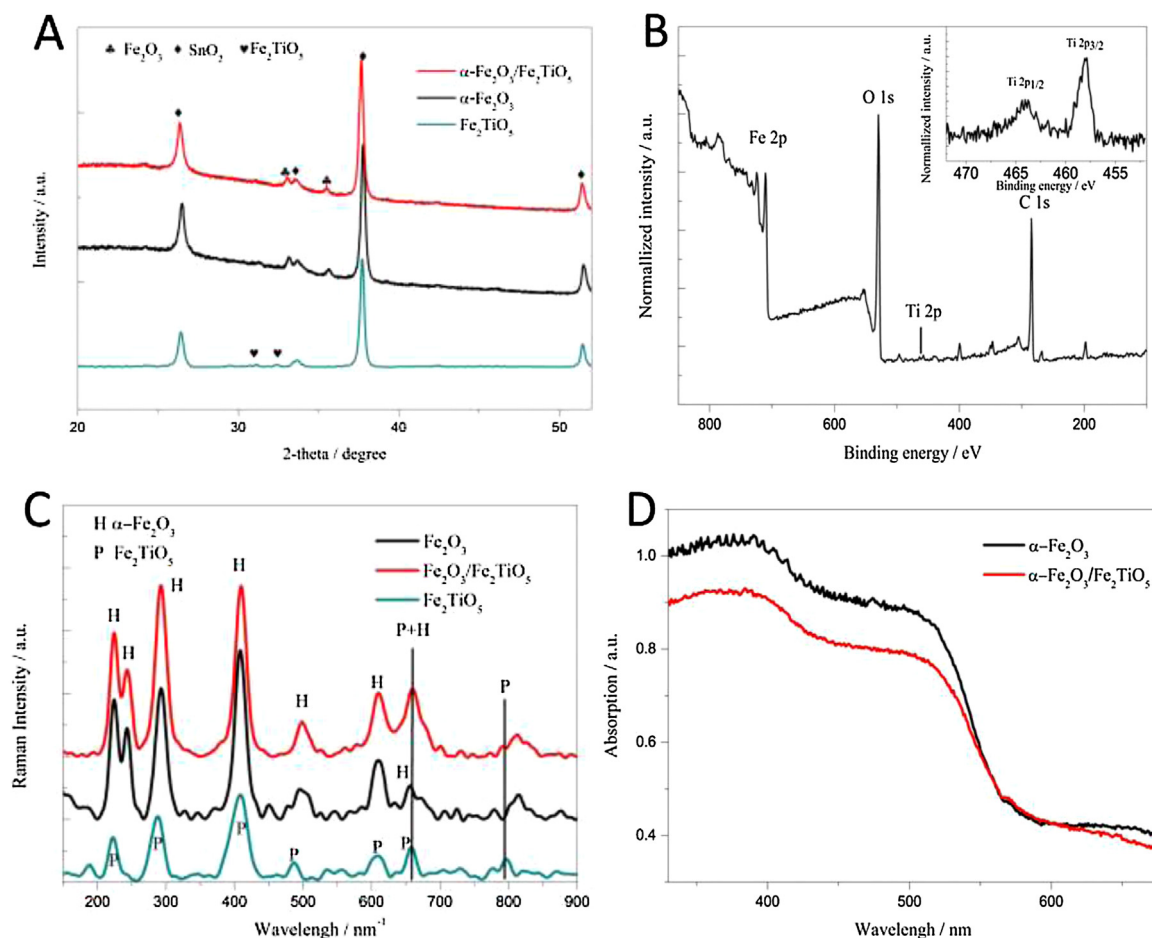
Fig. 3. (A) XRD patterns and (C) Raman spectra of α-Fe$_2$O$_3$, α-Fe$_2$O$_3$/Fe$_2$TiO$_5$ and Fe$_2$TiO$_5$. (B) XPS survey data of α-Fe$_2$O$_3$/Fe$_2$TiO$_5$. (D) UV–vis absorption spectra of α-Fe$_2$O$_3$ and α-Fe$_2$O$_3$/Fe$_2$TiO$_5$.
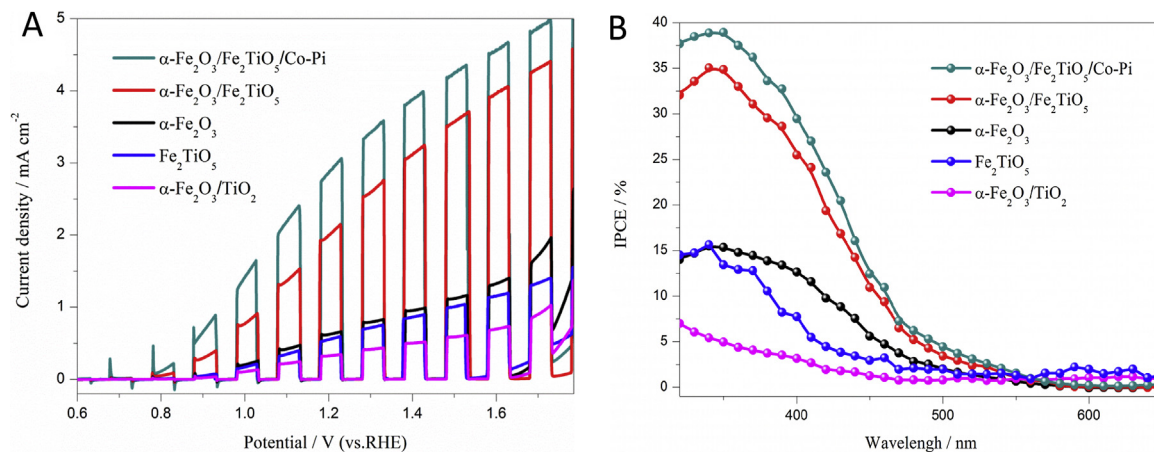
Fig. 4. (A) Photoelectrochemical responses of α-Fe$_2$O$_3$, α-Fe$_2$O$_3$/Fe$_2$TiO$_5$, α-Fe$_2$O$_3$/TiO$_2$, α-Fe$_2$O$_3$/Fe$_2$TiO$_5$/Co-Pi and Fe$_2$TiO$_5$ under chopped visible light illumination. (B) The IPCE responses of α-Fe$_2$O$_3$, α-Fe$_2$O$_3$/Fe$_2$TiO$_5$, α-Fe$_2$O$_3$/TiO$_2$ and α-Fe$_2$O$_3$/Fe$_2$TiO$_5$/Co-Pi.

fer to the surface. This finding further confirms the formation of Fe$_2$TiO$_5$ rather than TiO$_2$ in the α-Fe$_2$O$_3$/Fe$_2$TiO$_5$ sample. The application of cobalt phosphate (Co-Pi) can further enhance the photocurrent, resulting in values of ∼3.05 mA/cm^2 at 1.23 V *vs.* RHE. Additionally, reducing the onset potentials on α-Fe$_2$O$_3$/Fe$_2$TiO$_5$ and α-Fe$_2$O$_3$/Fe$_2$TiO$_5$/Co-Pi facilitates the water oxidation reaction occurring at the α-Fe$_2$O$_3$ surface. Note that the dark current densities show trends that apparently oppose those observed for the

chopped curves, possibly because of SSs redistribution or rebuilding because of adventitious Ti [31].

Fig. 4(B) shows the IPCE data of α-Fe$_2$O$_3$, α-Fe$_2$O$_3$/TiO$_2$, α-Fe$_2$O$_3$/Fe$_2$TiO$_5$ and α-Fe$_2$O$_3$/Fe$_2$TiO$_5$/Co-Pi. Based on Fig. 4B, we can better quantitatively assess the photoelectric conversion efficiency in the photoresponsive region. The IPCE responses of all samples occur between 340 nm and 590 nm, in line with the UV–vis absorption spectra shown in Fig. 6 and S5. The significant enhancement of α-Fe$_2$O$_3$/Fe$_2$TiO$_5$ and α-Fe$_2$O$_3$/Fe$_2$TiO$_5$/Co-Pi compared to α-Fe$_2$O$_3$
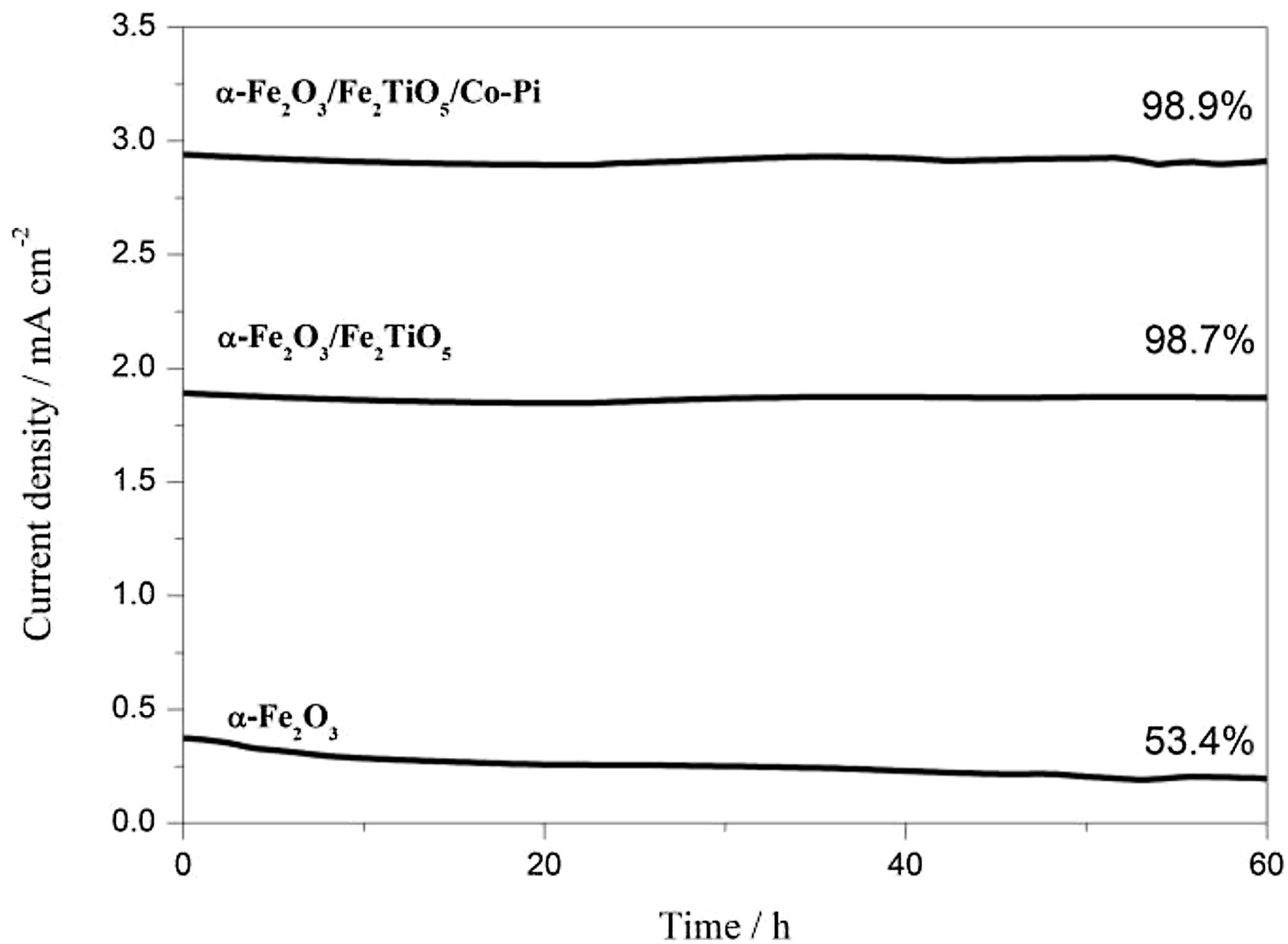
Fig. 5. Long-term photoresponse stabilities of α-Fe₂O₃, α-Fe₂O₃/Fe₂TiO₅, and α-Fe₂O₃/Fe₂TiO₅/Co-Pi under visible light illumination in 1-M KH₂PO₄ (pH = 7) at 1.23 V *vs.*RHE.

suggests that more carriers are transmitted to the surface for the same amount of photons, further confirming the significantly positive effect of the Fe$_2$TiO$_5$ layer (Fig. 4A). Clearly, α-Fe$_2$O$_3$/TiO$_2$ has the lowest IPCE value because of the unmatched band gap between Fe$_2$O$_3$ and TiO$_2$ (Fig. S6). To determine the stability of α-Fe$_2$O$_3$/Fe$_2$TiO$_5$ in PEC water splitting, the amperometric i-t curves of α-Fe$_2$O$_3$, α-Fe$_2$O$_3$/Fe$_2$TiO$_5$ and α-Fe$_2$O$_3$/Fe$_2$TiO$_5$/Co-Pi were continuously collected at 1.23 V vs. RHE in 1-M KOH (pH = 14) under standard illumination for 60 h (Fig. S7). The photocurrent densities of α-Fe$_2$O$_3$, α-Fe$_2$O$_3$/Fe$_2$TiO$_5$ and α-Fe$_2$O$_3$/Fe$_2$TiO$_5$/Co-Pi were 0.7, 2.0 and 3.05 mA/cm^2, respectively, and showed good stability and no significant attenuation; thus, these three photoanodes remain stable while the PEC system is operated under alkaline conditions. To pursue the idea of using Fe$_2$TiO$_5$, which possesses the excellent thermodynamic stability properties of TiO$_2$ in aqueous solutions [35], the amperometric i-t curves of the two optimized samples and pristine hematite (Fig. 5) were also collected at 0.6 V vs. Ag/AgCl in 1-M KH$_2$PO$_4$ (pH = 7). The α-Fe$_2$O$_3$/Fe$_2$TiO$_5$ and α-Fe$_2$O$_3$/Fe$_2$TiO$_5$/Co-Pi samples achieved a consistently photocurrent intensity of 2.0 mA/cm^2 in 60 h continuous operation without significant attenuation at 1.23 V vs. RHE, whereas the pristine hematite shows significant attenuation by 47.5% in photocurrent intensity from 0.62 mA/cm^2 to 0.32 mA/cm^2 throughout the course under the same bias potential. To explain the degradation mechanism of Fe$_2$O$_3$ and the protective role of Fe$_2$TiO$_5$, the SEM images of Fe$_2$O$_3$ and Fe$_2$O$_3$/Fe$_2$TiO$_5$ before (left) and after (right) long-term stability texts under neutral condition were taken. As shown in Fig. S12, the surface of Fe$_2$O$_3$ shows a corroded scene with some stripes, maybe causing by photocorrosion under neutral condition. However the surface of Fe$_2$O$_3$/Fe$_2$TiO$_5$ doesn't change significantly, suggesting that the existence of Fe$_2$TiO$_5$ could better protect Fe$_2$O$_3$. Also the fact that long-term stability text of Fe$_2$TiO$_5$ (Fig. S12) shows no significant attenuation well explained the protective role of Fe$_2$TiO$_5$. This means that the ultrathin Fe$_2$TiO$_5$ layer could broaden the scope of hematite application.

3.3. Hole dynamics process and surface states

As previously discussed, α-Fe$_2$O$_3$/Fe$_2$TiO$_5$ shows significantly enhanced photocurrent density, verified by its higher IPCE relative to that of pristine hematite. To further elucidate the role of Fe$_2$TiO$_5$, EIS was applied to the samples of α-Fe$_2$O$_3$, α-Fe$_2$O$_3$/Fe$_2$TiO$_5$ and α-Fe$_2$O$_3$/Fe$_2$TiO$_5$/Co-Pi. Fig. 6 shows the Nyquist plots of these samples at 1.23 V$_{RHE}$. Clearly, one large arc and another two small semicircles are evident in the impedance spectrum, demonstrating that the Fe$_2$TiO$_5$ layer can greatly decrease the resistance of α-Fe$_2$O$_3$ in PEC water splitting.

Generally, impedance reduction can be attributed to reduced electron-hole recombination rates, high carrier mobility and lifetime, and fast interfacial hole transfer at the surface, among other factors. However, which one plays a decisive role in how the Fe$_2$TiO$_5$ layer changes remains unknown. Therefore, obtaining a deeper understanding by applying a classical EC model, which directly divides carrier transmission processes into circuit elements and facilitates interpreting the EIS measurements, is necessary [36]. The EC requires the carrier trapping and charge transfer resistances and the corresponding capacitance, as shown in Fig. S7. Here, R$_S$ is the resistance of the electric contacts between the electrode and electrolyte. The next two parallel circuits represent direct hole transfer (through the valence band, DT) and indirect hole transfer (trapping holes at traps or SSs, IT), respectively [31]. In the DT process, C$_{bulk}$ refers to the capacitance of the charge accumulation in the bulk. For the IT process, R$_{trap}$ is the resistance of charge trapping at SS, whereas R$_{ct,ss}$ is the resistance of the charge transfer process from SS. Paralleling R$_{ct,ss}$, C$_{ss}$ accounts for the capacitance of charge accumulation on the SS. With the deposited
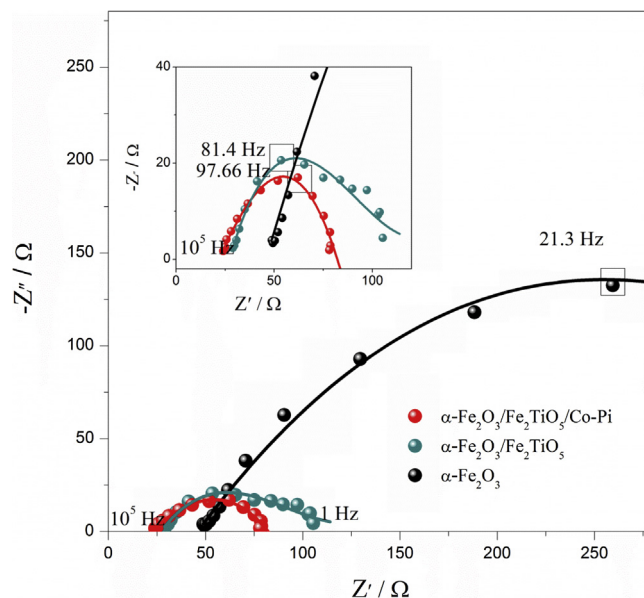

Fig. 6. EIS results of α-Fe$_2$O$_3$, α-Fe$_2$O$_3$/Fe$_2$TiO$_5$ and α-Fe$_2$O$_3$/Fe$_2$TiO$_5$/Co-Pi at 1.23 V vs. RHE. The lines represent best fittings of the experimental data to the equivalent circuit depicted in Fig. S8.

Fe$_2$TiO$_5$ coating layer, the charge transfer route will redistribute between DT and IT, and the values of all circuit elements will change. Fig. 7 shows the capacitance and resistance curves of α-Fe$_2$O$_3$, α-Fe$_2$O$_3$/Fe$_2$TiO$_5$ and α-Fe$_2$O$_3$/Fe$_2$TiO$_5$/Co-Pi with different voltages obtained by fitting their ECs. After Fe$_2$TiO$_5$ deposition, the resistance of α-Fe$_2$O$_3$/Fe$_2$TiO$_5$ generally decreases by approximately an order of magnitude more than that of α-Fe$_2$O$_3$, including R$_{trap}$ and R$_{ct,ss}$. In contrast, C$_{ss}$ increases, whereas C$_{bulk}$ decreases; thus, more carriers adopt the IT mode after redistribution. In addition, α-Fe$_2$O$_3$/Fe$_2$TiO$_5$ shows relatively low resistance and high capacitance compared to α-Fe$_2$O$_3$, in accordance with the photocurrent performance shown in Fig. 4(A). It is worth mentioning that the decrease in R$_{trap}$ suggests the improvement of the sluggish charge transfer kinetics of hematite, mainly because of heterojunction energy level matching and the diffusion model. Based on Fig. 7(D), when the values of R$_{ct,ss}$ are lower than those of α-Fe$_2$O$_3$, hole entrance into the electrolyte through SS is easier, which improves the poor charge transport properties of hematite. Note that C$_{ss}$and R$_{ct,ss}$ of α-Fe$_2$O$_3$/Fe$_2$TiO$_5$exhibit the reverse trend as the voltage increases, although the peak of C$_{ss}$ (onset potential, 0.9 V vs. RHE)and valley of R$_{ct,ss}$ (near the oxygen evolution potential, 1.23 V vs. RHE) do not correspond. Thus, the increasing number of carriers transferred through the SSs directly causes rapid photocurrent growth between the onset potential and oxygen evolution potential. As is known, Co–Pi can improve water oxidation kinetics on the photoanode surface during PEC water splitting, as verified by the green line of α-Fe$_2$O$_3$/Fe$_2$TiO$_5$/Co-Pi, where only the values of C$_{ss}$ and R$_{ct,ss}$ of α-Fe$_2$O$_3$/Fe$_2$TiO$_5$/Co-Pi show obvious changes. Therefore, the evident differences at low potentials (0.7-0.8 V vs. RHE) imply a lower onset potential, in line with Fig. 4A. Interestingly, the C$_{ss}$ value (green line) decreases rapidly in the initial stage, presenting a completely opposite trend compared with that of α-Fe$_2$O$_3$/Fe$_2$TiO$_5$ and implying that the holes are trapped at SS (the fastest process) at low potentials and then successively injected into the electrolyte through SS (the slower process).

3.4. Electron transfer efficiency

Because holes transfer through SSs contributes to improving photocurrent density, it is imperative to obtain further informa-
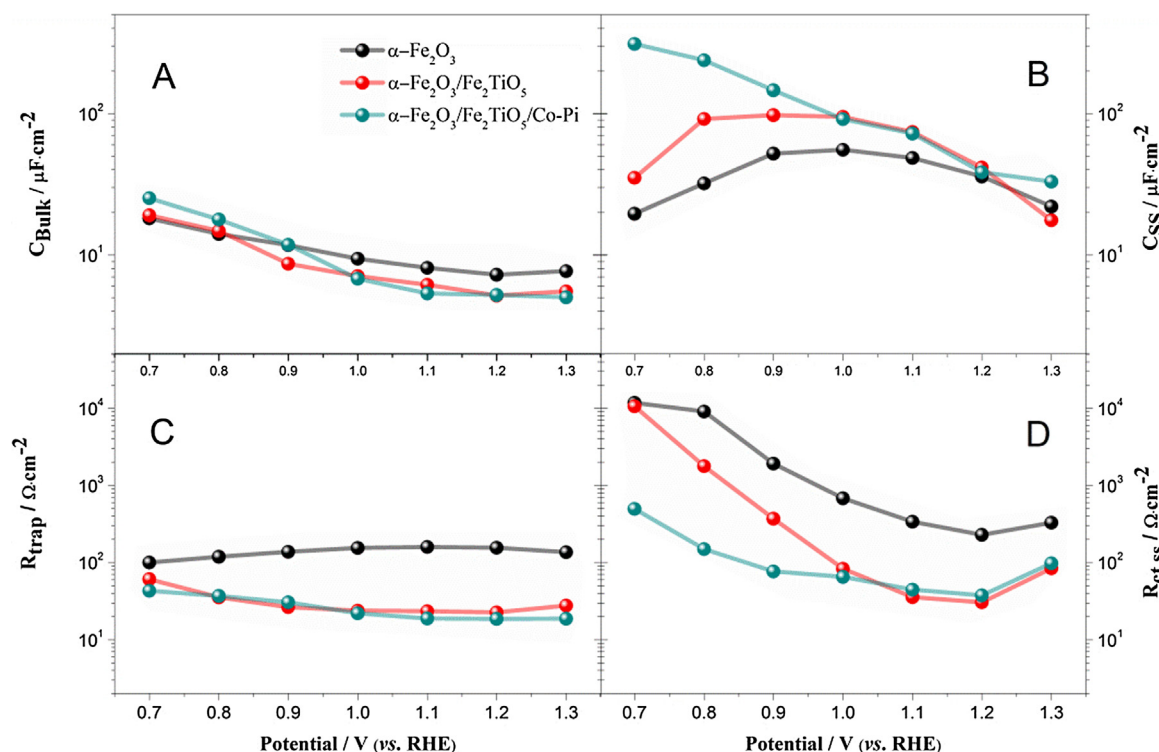
Fig. 7. Capacitances (top) and resistances (bottom) associated with the charge trapping (R_{trapp}, C_{bulk}) and transfer ($R_{ct,ss}$, C_{ss}) at/from SSs with different potentials and different samples (α-Fe$_2$O$_3$, α-Fe$_2$O$_3$/Fe$_2$TiO$_5$ and α-Fe$_2$O$_3$/Fe$_2$TiO$_5$/Co-Pi) obtained by fitting their ECs shown in Fig. S4. Error bars stem from the goodness of these fittings, each fitting error does not exceed 10%.

tion about electrons corresponding to the holes. The IMPS is a powerful method for understanding the semiconductor photo-generated carrier transport properties and obtaining information about carrier recombination. In this case, we use the concept of the average transit time required by photogenerated electrons to reach the back contact, which reflects the recombination probability of photogenerated electrons and holes. To further investigate the prepared α-Fe$_2$O$_3$/Fe$_2$TiO$_5$, IMPS was used to measure the charge transit times of as-prepared α-Fe$_2$O$_3$/Fe$_2$TiO$_5$ above and α-Fe$_2$O$_3$/Fe$_2$TiO$_5$ synthesized through FeOOH (use same Ti-treatment as mentioned in 2.2), which are denoted as Fe-Fe$_2$O$_3$/Fe$_2$TiO$_5$ and FeOOH-Fe$_2$O$_3$/Fe$_2$TiO$_5$, respectively. The transit time τ_D can be calculated by the formula $\tau_D = (2\pi f_{min})^{-1}$, where &z.hfl;$_{min}$ is the characteristic frequency at which the minimum value occurs in the IMPS plot [37].

As shown in Fig. 8(A), the f_{min} values of the two samples are 33 Hz and 53 Hz. According to the formula, we can obtain the τ_D values of traditional α-Fe$_2$O$_3$/Fe$_2$TiO$_5$ and as-prepared α-Fe$_2$O$_3$/Fe$_2$TiO$_5$: 4.822 ms and 3.004 ms, respectively. After eliminating the factor of thickness (~195 nm), the results suggest that the photogenerated electrons of as-prepared α-Fe$_2$O$_3$/Fe$_2$TiO$_5$ are more likely to reach the back contact than those of traditional α-Fe$_2$O$_3$/Fe$_2$TiO$_5$. Since the nanostructured defects and unwanted impurities in the as-prepared α-Fe$_2$O$_3$/Fe$_2$TiO$_5$ synthesized through Fe film are absent mentioned above, the electron transform here is faster, leading to a higher current density compared to traditional α-Fe$_2$O$_3$/Fe$_2$TiO$_5$.

The IMPS plots of α-Fe$_2$O$_3$, α-Fe$_2$O$_3$/Fe$_2$TiO$_5$, α-Fe$_2$O$_3$/TiO$_2$ and α-Fe$_2$O$_3$/Fe$_2$TiO$_5$/Co-Pi are also shown in Fig. S11. According to the obtained frequency information, it can be calculated that the τ_D values are 7.958 ms, 6.121 ms, 3.004 ms and 2.307 ms, respectively. The electron transport rate clearly presents a similar trend to the photoelectric response (Fig. 4), revealing that ultrathin heterojunction and surface modification enhance the electron transport rate

and reduce charge recombination. Note that α-Fe$_2$O$_3$/TiO$_2$ shows a longer τ_D value compared to α-Fe$_2$O$_3$, although the conduction band of α-Fe$_2$O$_3$/TiO$_2$ is conducive to electronic transmission (Fig. S6). The unmatched valence band leads to improved charge recombination which offsets the positive effect of conduction band to electron.

To further explain carrier transfer information about hematite, a hypothetical M-S structure is used for Fe$_2$O$_3$/Fe$_2$TiO$_5$, which referred to the analytical method of some of the literature when an ultra-thin layer heterojunction formed[21]. The following equation: $N_d = (2/e\varepsilon\varepsilon_0)[d(1/C^2)/dV]^{-1}$, where N_d is the charge donor density, e is the electron charge, ε is the relative dielectric constant of hematite ($\varepsilon = 60$), ε_0 is the permittivity of vacuum (8.85×10^{-12} F m^{-1}), and V is the applied bias at the electrode [31]. As shown in Fig. 8(B), the presence of Fe$_2$TiO$_5$ significantly decreases the slope, indicating the rapid growth of N_d according to the equation, in accord with the calculated electron densities of α-Fe$_2$O$_3$ and α-Fe$_2$O$_3$/Fe$_2$TiO$_5$ (8.39337×10^{19} cm^{-3} and 2.03197×10^{21} cm^{-3}, respectively). Note that the electron density of Fe-Fe$_2$O$_3$ is increased compared to FeOOH-Fe$_2$O$_3$, mainly because of the fewer nanostructured defects in prepared α-Fe$_2$O$_3$ compared to hematite synthesized through FeOOH. The Mott–Schottky conclusion reveals a further explanation for an improved carrier density due to defects and introduction of ultra-thin Fe$_2$TiO$_5$, which is consistent with IMPS conclusions, indicating that the use of M–S structure can seem to further explain the electron migration to some extent.

Based on the carrier transfer information obtained here, we can create a carrier transfer model of an ultrathin film deposited uniform hematite using our preparation method. According to Fig. 8B, the V_{fb}s of Fe$_2$O$_3$ and Fe$_2$TiO$_5$ are determined to be 0.47 and 0.39 V vs RHE, respectively. Assuming that the gap between the V_{fb} and the bottom edge of the conduction band is small (~0.2 eV), the conduction band position of Fe$_2$O$_3$ and Fe$_2$TiO$_5$ could be identi-
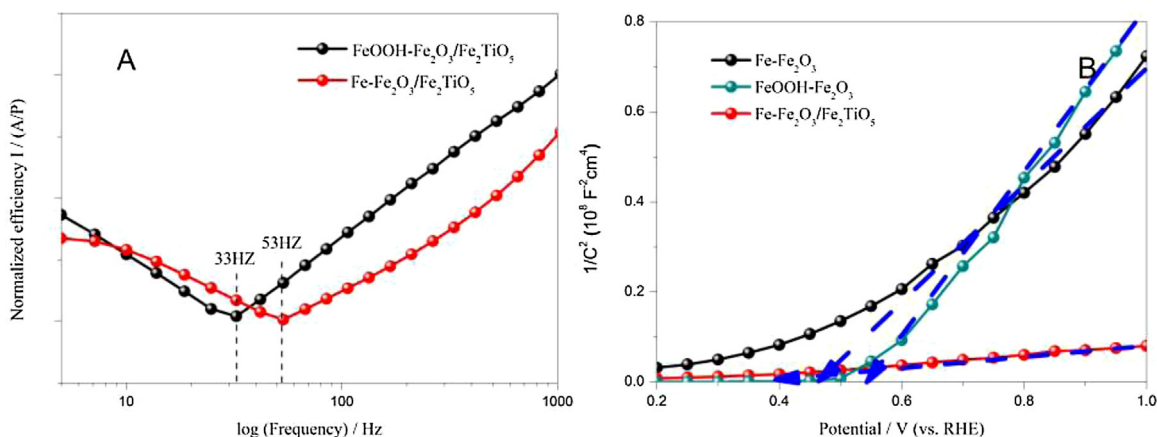
Fig. 8. (A) The IMPS plots of Fe-Fe$_2$O$_3$/Fe$_2$TiO$_5$ (preparaed by Fe) and FeOOH-Fe$_2$O$_3$/Fe$_2$TiO$_5$ (preparaed by FeOOH). (B) Mott–Schottky plots for Fe-Fe$_2$O$_3$, FeOOH-Fe$_2$O$_3$ and Fe-Fe$_2$O$_3$/Fe$_2$TiO$_5$ in the dark.
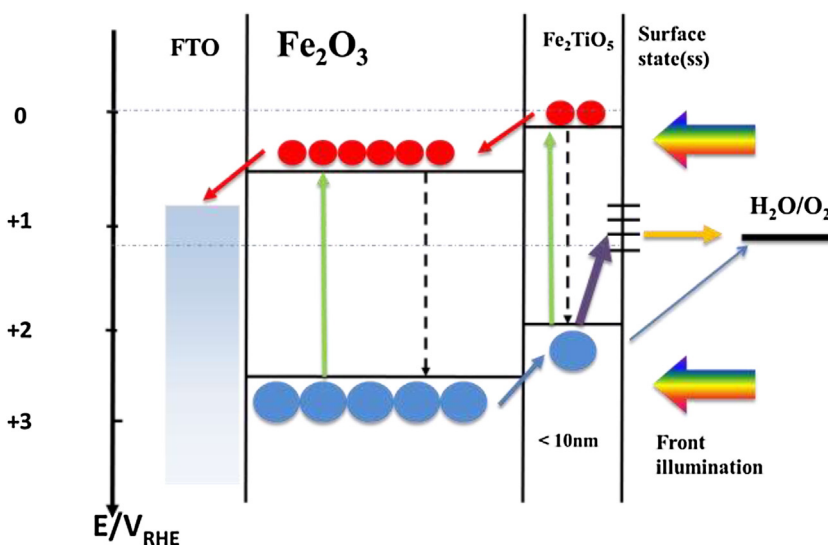
Fig. 9. The band structure of α-Fe$_2$O$_3$/Fe$_2$TiO$_5$.

fied as ∼0.3 v and ∼0.2 v, respectively. By considering the bandgap energy from the ultraviolet visible absorption spectra (Fig. 3D), the valence band position also could be confirmed (Fig. 9). Hence, the geometric model is created using front illumination (Fig. 9), and the band structure of α-Fe$_2$O$_3$/Fe$_2$TiO$_5$ ensures that photocarriers transfer smoothly along the energy band (red and blue arrow), ameliorating the effects of the short carrier lifetime and short hole diffusion length of hematite, as verified by the value of R$_{trap}$ shown in Fig. 7(C). Besides, less microstructural defects of hematite results in faster charge transfer (orange arrow) confirmed by the transit time (τ_D) and charge carrier density (N$_d$), which increase the conductivity and decrease the impedance of the photoanode. In this case, the photogenerated electron-hole pairs are effectively separated. Furthermore, it is worth mentioning that the ultrathin Fe$_2$TiO$_5$ film ($\ll$10 nm) facilitates the photogenerated hole diffusion to the SSs (purple arrow) compared to direct bulk transport (blue arrow), implying that a larger percentage of charges locate on SS, as verified by the value of CSS shown in Fig. 7(B). Thus, the presence of an ultrathin film shortens the diffusion layer width and further strengthens the function of SSs, and as a result, the surface kinetics plays a vital role throughout the carrier transfer process. That is the reason why the deposition of Co-Pi could increase the photocurrent density of α-Fe$_2$O$_3$/Fe$_2$TiO$_5$ from 2.0 to 3.05 mA/cm^2. Also other mature oxidized intermediates could be used to further

enhance the surface kinetics. Finally, the Fe$_2$TiO$_5$ layer could play a protective role for the hematite because of its excellent thermo-dynamic stability. These three aspects could alter the competition between carrier migration and recombination and stable operation in the PEC system. Our work could inspire new preparation methods for semiconductor modification toward efficient water oxidation.

4. Conclusion

In this work, through a simple and in situ method, a Fe/TT structure was successfully constructed by direct ER and the sol method and then was converted to α-Fe$_2$O$_3$/Fe$_2$TiO$_5$ after thermal treatment. TEM, XPS, and Raman techniques indicated the formation of a Fe$_2$TiO$_5$ layer on the hematite. The as-prepared photoanode showed a higher photocurrent density of ∼2.0 mA/cm^2, and Co-Pi photodeposition further enhanced the photocurrent density to ∼3.05 mA/cm^2 and the IPCE to ∼40%. The EIS analysis indicated that the presence of the ultrathin Fe$_2$TiO$_5$ layer effectively reduced the photocarrier recombination and enhanced the surface states density. Most holes indirectly transferred to the surface states because of the shorter diffusion distance of the Fe$_2$TiO$_5$ layer. The ultrathin α-Fe$_2$O$_3$/Fe$_2$TiO$_5$ film achieved a consistently photocurrent intensity in 60 h continuous operation. The IMPS and Mott-Schottky

plots revealed the conductivity improvement of samples resulting from the uniform and orderly hematite. Therefore, this novel facile method could greatly improve the performance of hematite for solar water oxidation and allow for large-scale preparation

Acknowledgements

Appendix A. Supplementary data

Supplementary data associated with this article can be found, in the online version, at http://dx.doi.org/10.1016/j.apcatb.2017.07.012.

References

[1] C.C. Wang, J.R. Li, X.L. Lv, Y.Q. Zhang, G. Guo, Energy Environ. Sci. 7 (2014) 2831–2867.
[2] A. Fujishima, K. Honda, Nature 238 (1972) 37–38.
[3] A.A. Ismail, D.W. Bahnemann, Sol. Energy Mat. Sol. C 128 (2014) 85–101.
[4] S. Ahmed, M.G. Rasul, W.N. Martens, R. Brown, M.A. Hashib, Desalination 261 (2010) 3–18.
[5] M.D. Bhatt, J.S. Lee, J. Mater. Chem. A 3 (2015) 10632–10659.
[6] K. Nakata, A. Fujishima, J. Photochem. Photobiol. C- Photochem. Rev. 13 (2012) 169–189.
[7] C. Janáky, K. Rajeshwar, N.R. de Tacconi, W. Chanmanee, M.N. Huda, Catal. Today 199 (2013) 53–64.
[8] K. Sivula, F. Le Formal, M. Gratzel, ChemSusChem 4 (2011) 432–449.
[9] A. Duret, M. Grätzel, J. Phys. Chem. B 109 (2005) 17184–17191.
[10] H. Zhang, L. Zhou, C. Yu, RSC Adv. 4 (2014) 495–499.
[11] G.M. Wang, Y.C. Ling, D.A. Wheeler, K.E.N. George, K. Horsley, C. Heske, J.Z. Zhang, Y. Li, Nano Lett. 11 (2011) 3503–3509.
[12] A. Murphy, P. Barnes, L. Randeniya, I. Plumb, I. Grey, M. Horne, J. Glasscock, Efficiency of solar water splitting using semiconductor electrodes, Int. J. Hydrogen Energy 31 (2006) 1999–2017.
[13] S.D. Tilley, M. Cornuz, K. Sivula, M. Gratzel, Angew. Chem. Int. Ed. 122 (2010) 6549–6552.
[14] F.E. Osterloh, Chem. Soc. Rev. 42 (2013) 2294–2320.
[15] X. Lian, X. Yang, S. Liu, Y. Xu, C. Jiang, J. Chen, R. Appl. Surf. Sci. 258 (2012) 2307–2311.
[16] R. Franking, L. Li, M.A. Lukowski, F. Meng, Y. Tan, R.J. Hamers, S. Jin, Energy Environ. Sci. 6 (2013) 500–512.
[17] C. Miao, T. Shi, G. Xu, S. Jin, C. Ye, ACS Appl. Mater. Interfaces 5 (2013) 1310–1316.
[18] X. Yang, R. Liu, C. Du, P. Dai, D. Zheng, ACS Appl. Mater. Interfaces 6 (2014) 12005–12011.
[19] J.J. Deng, X.X. Lv, J.Y. Liu, H. Zhang, K.Q. Nie, C.H. Hong, J.O. Wang, X.H. Sun, J. Zhong, S.T. Lee, ACS Nano 9 (2015) 5348–5356.
[20] M.T. Mayer, Y. Lin, G. Yuan, D. Wang, Acc. Chem. Res. 46 (2013) 1558–1566.
[21] Q. Liu, J. He, T. Yao, Z. Sun, W. Cheng, S. He, Y. Xie, Y. Peng, H. Cheng, Y. Sun, Y. Jiang, F. Hu, Z. Xie, W. Yan, Z. Pan, Z. Wu, S. Wei, Nat. Commun. 5 (2014) 5122.
[22] C. Li, T. Wang, Z. Luo, S. Liu, J. Gong, Small 12 (2016) 3415–3422.
[23] P.S. Bassi, R.P. Antony, P.P. Boix, Y. Fang, J. Barber, L.H. Wong, Nano Energy 22 (2016) 310–318.
[24] Q.Y. Zeng, J. Bai, J.H. Li, L.G. Xia, K. Huang, X.J. Li, B.X. Zhou, J. Mater. Chem. A 3 (2015) 4345–4353.
[25] H. Kozuka, M. Kajimura, J. Sol-Gel Sci. Techn. 22 (2001) 125–132.
[26] S.M. Guo, S.Y. Wang, N.N. Wu, J.R. Liu, Y.X. Ni, W. Liu, RSC Adv. 5 (2015) 103767–103775.
[27] A.P. Grosvenor, B.A. Kobe, M.C. Biesinger, N.S. McIntyre, Surf. Interface Anal. 36 (2004) 1564–1574.
[28] D. Briggs, J. C. Riviere, John Wiley & Sons, 1983, 1–647.
[29] D.L.A. De Faria, S. Venâncio Silva, M.T. De Oliveira, J. Raman Spectrosc. 28 (1997) 873–878.
[30] S. Wang, W. Wang, W. Wang, Z. Jiao, J. Liu, Y. Qian, Sens. Actuators B-Chem. 69 (2000) 22–27.
[31] D. Monllor-Satoca, M. Bärtsch, C. Fàbrega, A. Genç, S. Reinhard, T. Andreu, J. Arbiol, J. Niederberger, J.R. Morante, Energy Environ. Sci. 8 (2015) 3242–3254.
[32] P.H.C. Camargo, G.G. Nunes, G.R. Friedermann, D.J. Evans, G.J. Leigh, G. Tremiliosi-Filho, E.L. de Sá, A.J.G. Zarbin, J.s.F. Soares, Mater. Res. Bull. 38 (2002) 1915–1928.
[33] L.B.M. Lopez, J.D. Pasteris, P. Biswas, Appl. Spectrosc. 63 (2009) 627–635.
[34] D. Bersani, P.P. Lottici, A.A. Montenero, J. Mater. Sci. 35 (2000) 4301–4305.
[35] P.S. Bassi, L.H. Wong, J. Barber, Phys. Chem. Chem. Phys. 16 (2014) 11834–11842.
[36] B. Klahr, S. Gimenez, F. Fabregat-Santiago, T. Hamann, J. Bisquert, J. Am. Chem. Soc. 134 (2012) 4294–4302.
[37] J. Su, L. Guo, N. Bao, C.A. Grimes, Nano Lett. 11 (2011) 1928–1933.